Thermite synthesis and characterization of Co–ZrO$_2$ferromagnetic nanocomposite thin films

V.G. Myagkov [a, *], V.S. Zhigalov [a, b], L.E. Bykova [a], S.M. Zharkov [a, c], A.A. Matsynin [a, c], M.N. Volochaev [a, b], I.A. Tambasov [a], G.N. Bondarenko [d]

[a] *Kirensky Institute of Physics, Russian Academy of Sciences, Siberian Branch, Krasnoyarsk, 660036, Russia*
[b] *Reshetnev Siberian State Aerospace University, Krasnoyarsk, 660014, Russia*
[c] *Siberian Federal University, Krasnoyarsk, 660041, Russia*
[d] *Institute of Chemistry and Chemical Technology, Russian Academy of Sciences, Siberian Branch, Krasnoyarsk, 660049, Russia*

ABSTRACT

Co–ZrO$_2$ ferromagnetic nanocomposite thin films were successfully synthesized using a new thermite reaction between Zr and Co$_3$O$_4$ in layer geometry. The initial Zr/Co$_3$O$_4$ bilayers were obtained by the deposition of Zr layers onto Co$_3$O$_4$ films at room temperature. The process of mixing at the Zr/Co$_3$O$_4$ interface and synthesis of fine-crystalline Co and amorphous ZrO$_2$ phases started at a temperature above the initiation temperature T$_{in}$ ~250 °C which did not depend on the bilayer thickness. For the bilayer thickness more than 300 nm high-temperature fcc-Co and cubic c-ZrO$_2$ (or tetragonal t-ZrO$_2$) phases were formed. For the bilayer thickness less than ~50 nm stable low-temperature hexagonal hcp-Co and monoclinic m-ZrO$_2$ phases were also present in the reaction product. A partial transformation from Co$_3$O$_4$ to CoO occurred after annealing at 300 °C. The secondary reaction between CoO and Zr started soon after Co$_3$O$_4$ had been converted to the CoO phase. After annealing at 500 °C more than 80% of Co was reduced and the final product contained Co nanoparticles above and below the superparamagnetic critical size embedded into a dielectric ZrO$_2$ matrix. The synthesized Co–ZrO$_2$ nanocomposite films possessed soft magnetic behavior, high magnetization and good chemical stability.

© 2016 Elsevier B.V. All rights reserved.

1. Introduction

Granular solids composed of ferromagnetic nanoparticles embedded in semiconducting (e.g. In$_2$O$_3$, TiO$_2$, ZnO, SnO$_2$) and insulating (e.g. SiO$_2$, Al$_2$O$_3$, MgO, HfO$_2$, ZrO$_2$) matrices have attracted a great deal of attention, both from the point of view of the fundamental perspective and for their potential applications [1–3]. These nanocomposites display magnetic and physicochemical properties which strongly depend on the method of preparation, the particle size, concentration and chemical bonding between the nanoparticles and matrix. Many approaches have been developed to synthesize ferromagnetic nanoparticles in semiconducting and insulating matrices such as the sol–gel method [4–6], rf magnetron sputtering [7–9], thermal decomposition [10], ball milling [11,12], etc. Among the above mentioned oxides ZrO$_2$ is a well known ceramic material which possesses excellent thermal,

electric, mechanical, optical properties, good chemical stability and has many practical applications [13–17]. The fabrication of ZrO$_2$-based ferromagnetic nanocomposites is a challenging goal, as this can provide ZrO$_2$ with the magnetic properties, which considerably enhance possibilities for applications. In the literature a major part of the papers is directed towards elucidating the nature of magnetism in transition metal doped ZrO$_2$ [18–20] and stabilization of the high temperature crystalline tetragonal (t-ZrO$_2$) and cubic (c-ZrO$_2$) phases [21–23]. Although ZrO$_2$-based magnetic nanocomposites obtained by various methods have been widely investigated, only a few reports are directed towards investigating magnetic, optical, magneto-optical, AC conductance and magnetoresistance properties in Co–ZrO$_2$ granular thin films [24–28]. The only method currently used for the fabrication of Co–ZrO$_2$ granular thin films is pulsed laser deposition. These films had an average Co nanoparticle size of about 2.5–63 nm against the Co volume fraction and showed a very sharp interface between the crystalline Co nanoparticles and the amorphous ZrO$_2$ matrix, with no evidence of intermixing [24–26]. Increasing the annealing temperature up to

400 °C lead to the modification of the granular structure, which resulted in both the nucleation of ultra-small particles and the coalescence of neighboring particles [27]. In addition, J. Shin et al. reported the formation of magnetic nanostructures from self-assembled Co nanodots and nanowires embedded in a yttria-stabilized zirconia matrix which had been grown on Si(001) at 800 °C and 5×10^{-4} Torr O_2 pressure [28].

Recently, we have demonstrated a new thermite method for synthesizing ferromagnetic Fe–In_2O_3 [29] and Fe–ZrO_2 [30] nanocomposite films containing α-Fe clusters embedded into a transparent conducting In_2O_3 oxide and dielectric ZrO_2 matrix, respectively. In this report, we extend this approach to the formation of magnetic Co–ZrO_2 nanocomposites using a new thermite reaction (1):

$$Co_3O_4 + 2Zr = 2ZrO_2 + 3Co \qquad (1)$$

Thermite reactions between fuels such as Al, Be, Mg, B, Hf, Li, Ta, Ti, Zr and oxidizers such as SiO_2, SnO_2, WO_3, MoO_3, CuO, Bi_2O_3, I_2O_5, Cr_2O_3, Fe_2O_3 react with a release of large quantities of heat, may have a self-propagating high-temperature synthesis (SHS) mode and widely used for the synthesis of materials. For traditional thermites which contain micron-sized particles, the combustion velocity is of the order of several centimeters to a few meters per second [31]. When a fuel and oxidizer particles decease to nano-scale dimensions the combustion velocity drastically increases to several km/s [32,33]. These nanocomposite thermites (also termed nanostructured metastable intermolecular composites, nano-thermites or superthermites) often have free-standing multilayer foil geometry [34–37]. In contrast to free-standing multilayer thermites in reactive bilayer films coupled with a substrate which is the major heat sink during the reaction, the combustion wave occurs when the temperature of a sample T_S exceeds the initiation temperature T_{in} ($T_S > T_{in}$) and heating rate is higher than 20 K/s [29,30]. At a heating rate less then 20 K/s the reaction occurs by low reactive diffusion across the entire interface.

In this work, we describe the low-temperature thermite synthesis of Co–ZrO_2 nanocomposite films containing Co nanoclusters separated by ZrO_2 grains. The final goal was to elucidate structural and magnetic transformations formed in the Zr/Co_3O_4 bilayers after thermal annealing from 50 to 500°C.

2. Experimental section

2.1. Synthesis

The initial films were obtained by the thermal deposition of Co layers at a temperature of 250 °C onto NaCl(001) and chemically pure glass substrates having a thickness of 0.18 mm in vacuum at a residual pressure of 10^{-6} Torr. Previously, the substrates were degassed at 350 °C for 1 h. The Co_3O_4 films were obtained by oxidation in an air environment of the initial Co films at a temperature of ~350 °C. The top Zr layer was deposited at room temperature to prevent a reaction between Zr and Co_3O_4 during the deposition. In these experiments, Zr/Co_3O_4 bilayers with an approximate stoichiometry Co:Zr = 3:2 were used. The films on NaCl(001) with the thicknesses of Co equal to 20 nm and Zr - 30 nm were prepared for transmission electron microscopy (TEM) and in situ heating electron diffraction studies. In the rest of the experiments films on the glass substrates with a total thickness of 300–400 nm were used. Magnetic, electrical and TEM studies were conducted on Zr/Co_3O_4 bilayers annealed at temperatures between 50 and 500 °C at 50 °C intervals. The samples were held at each temperature for 1 h. All the synthesized Co–ZrO_2 samples were obtained at a pressure of 10^{-6} Torr. In situ TEM experiments were

performed by heating the Zr/Co_3O_4 films in the column of the JEM-2100 transmission electron microscope (JEOL) using a sample holder with an option of the controlled heating from room temperature to 1000 °C (Gatan Model 652 Double Tilt Heating Holder). The Zr/Co_3O_4 films were separated from the substrate and placed on a molybdenum TEM grid. Electron diffraction data of the in situ heating experiments was captured during the experiments.

2.2. Characterization

The phases formed during the synthesis process were identified using a DRON-4007 X-ray diffractometer (Cu K$_\alpha$ radiation). The thicknesses of the Zr and Co_3O_4 layers were determined via X-ray fluorescent analysis. The saturation magnetization M_S, in-plane hysteresis loops and magnetic moment of the samples were measured by a vibrating magnetometer and were also controlled by torque measurements which had been described in detail in our previous work [38]. For finding the Co reduction degree $\eta(T_S)$ versus annealing temperature T_S the magnetic moment $M_S^{Co}V_0$ of the initial (before oxidation) Co film with V_0 volume was measured. The degree of Co reduction $\eta(T_S)$ was obtained using Formula (2):

$$\eta(TS) = M_S^{Co}V(TS)/M_S^{Co}V_0 = V(TS)/V_0 \qquad (2)$$

where $V(T_S)$ is Co reduction volume after annealing at temperature T_S.

The resistance $R(T_S)$ measurements were performed by a standard four-probe method in a vacuum of 10^{-6} Torr while the as-deposited Zr/Co_3O_4 bilayer annealed at a constant heating rate of 4 °C/min from room temperature up to 500 °C, and then cooling at a rate of ~3 °C/min to room temperature. Magnetoresistance measurements were carried out at room temperature in the magnetic field up to 4.5 kOe by using the standard four-probe technique.

3. Results and discussion

3.1. Synthesis characterization

The initial Co films had saturation magnetization (M_S^{Co} = 1400 emu/cm^3) coinciding with the saturation magnetization of the bulk samples. The samples were oxidized in air for the formation of a Co_3O_4 phase which had zero magnetization. To avoid a reaction between Zr and Co_3O_4, the initial Zr/Co_3O_4 bilayers were obtained from the deposition of a Zr layer on the Co_3O_4 film at room temperature. The magnetization M_S of the samples did not change after the deposition of the Zr layer.

Fig. 1 shows the Co reduction degree $\eta(T_S)$ and electrical resistance $R(T_S)$ as a function of annealing temperature T_S for the Zr/Co_3O_4 bilayers. Up to 250 °C the saturation magnetization M_S of the Zr/Co_3O_4 bilayers remained equal to zero ($\eta = 0$), which indicated that there was no mixing and reaction between the Zr and Co_3O_4 layers. With the increasing annealing temperature above 250 °C, the reduction degree η strongly increased up to 300 °C and gradually reached a maximum of η ~0.8 at 500 °C (Fig. 1a). From this it follows that Reaction (1) had the initiation temperature T_{in} ~250 °C and more than 80% of Co was reduced by Zr. Fig. 1b shows the electrical resistance $R(T_S)$ versus annealing temperature T_S for the Zr/Co_3O_4 bilayers which were heated at a rate of 4 °C/min to 500 °C and cooled to room temperature. The temperature increase above T_{in} = 250 °C led to a rapid increase in electrical resistance, which was undoubtedly due to the initiation at T_{in} = 250 °C and development of Reaction (1). The rapid increasing of the electrical resistance was associated with the formation of the insulating ZrO_2 matrix. After annealing from 300 °C to 400 °C the electrical resistance decreased, which was associated with the continuum
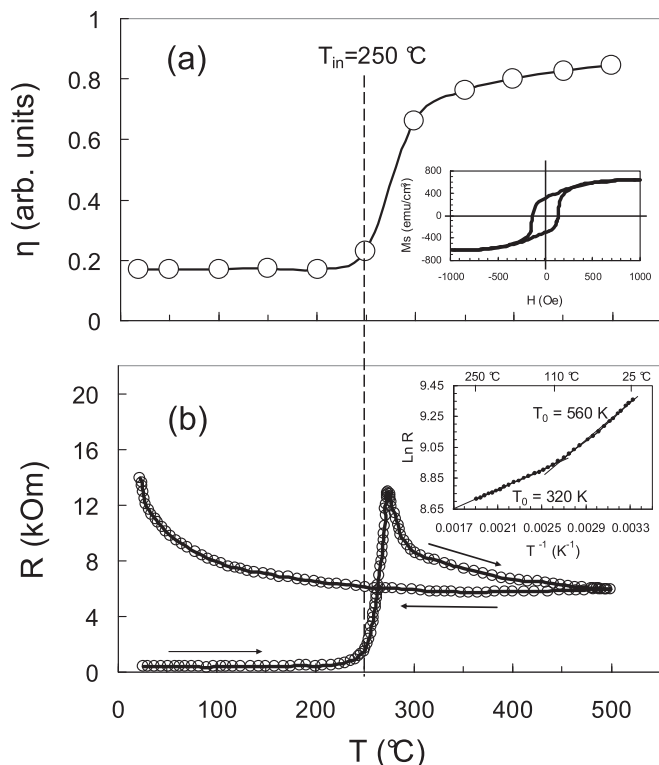
Fig. 1. (a) The degree of Co reduction η as a function of annealing temperature T_S for the Zr/Co$_3$O$_4$ bilayers. The inset shows the room temperature hysteresis loop of the synthesized Co− ZrO$_2$ nanocomposite after annealing at 500 °C. (b) Electrical resistance of the Zr/Co$_3$O$_4$ bilayers heated up to 500 °C (the heating rate being 4 °C/min) as a function of temperature measurement T_S. The inset shows the ln R vs −T^{-1} plot for the as-synthesized Co− ZrO$_2$ sample after cooling in the 250 °C - 25 °C temperature interval.

reaction (1) and the growth of the Co nanoparticles, which increased the conductivity via an insulating ZrO$_2$ matrix. Above 400 °C − 500 °C the electrical resistance weakly depended on the annealing temperature and it is assumed that the reaction between Zr and Co$_3$O$_4$ had been completed at 500 °C. As the temperature decreased below 500 °C samples began to show metallic-like behavior. The decreasing electrical resistance was most likely associated with the Co grain growth, which eventually formed a percolation cluster in the dielectric ZrO$_2$ matrix. As the synthesized Co−ZrO$_2$ samples cooled to the initiation temperature T$_{in}$ ~250 °C the post-reaction processes continued and promoted the insulation of the Co nanoparticles by ZrO$_2$ and the start of the increase of the electrical resistance. Upon cooling below 250 °C to room temperature the resistance showed a strong temperature dependence, and it is assumed that the Co−ZrO$_2$ films were in the insulating conduction regime. For the insulating regime in metal granular films the resistivity R versus temperature T is described by Eq. (3) [1,39−41].

$$R(T) = R_0 \exp\left[(T_0/T)^n\right] \qquad (3)$$

Where n = 1 indicates the thermal activation conduction, n = 1/2 tunneling, and n = 1/4 Mott variable range hopping. The optimal fitting of the experimental data of the Co−ZrO$_2$ film has the exponent n = 1 for two temperature regions: 20 °C − 110 °C (T$_0$ = 560 K, E$_a^1$ = 0.048 eV) and 110 °C − 250 °C (T$_0$ = 560 K, E$_a^2$ = 0.0275 eV). The ln R against -T^{-1} plot is given in the inset of Fig. 1b. In both cases the dominant conduction mechanism is thermally activated conduction. One conceivable reason for the low

electrical resistance activation energy is the result of recrystallization and coarsening of Co and ZrO$_2$ grains, which can occur in the 110 °C - 250 °C temperature interval. After structural relaxation in the as-synthesized Co−ZrO$_2$ film in the 110 °C − 20 °C temperature interval the as-synthesized Co−ZrO$_2$ films had an activation energy that is typical for metal granular films at these temperatures [41].

It is significant that only 20% of the Co atoms were not included into the synthesizing metallic Co nanoclusters. Most likely they remained in the unreacted Co$_3$O$_4$ and CoO oxides or in the ZrO$_2$ solid solution, which formed at Co/ZrO$_2$ interface during Reaction (1) as the transition zone between the Co nanoclusters and ZrO$_2$ matrix.

3.2. XRD and TEM characterizations

The X-ray diffraction (XRD) pattern of the initial Zr/Co$_3$O$_4$ bilayers contained reflections from the fine-dispersed polycrystalline Zr and Co$_3$O$_4$ phases (Fig. 2a). After annealing at 300 °C the weak reflections from Co$_3$O$_4$ disappeared and a new peak (111) of high-temperature c-ZrO$_2$ (or t-ZrO$_2$) phase was formed (Fig. 2b). The c-ZrO$_2$ and t-ZrO$_2$ (in the paper c/t-ZrO$_2$) phases had the proximity of the related peaks and so, these phases are unambiguously distinguished using only conventional X-ray diffraction. The lack of Co peeks implies that in the initial stage Co was fine-crystalline. Upon annealing at 500 °C the X-ray patterns contained (111), (200), (311), (400) c/t-ZrO$_2$ reflections and (111), (200), (220) reflections of the high-temperature fcc-Co and no peaks from the stable low-temperature hexagonal hcp-Co and monoclinic m-ZrO$_2$ phases (Fig. 2c). The difference in the binding energies of cobalt in the hexagonal and cubic modifications is insignificant; therefore in thin films and nanostructures the fcc-Co phase is often stabilized.

Fig. 3a shows the sand-like microstructure of the top Zr layer of the initial Zr/Co$_3$O$_4$ bilayer, which indicates that the crystalline size of Zr grains is very low (<5 nm). These data are compared with the XRD average crystallite size ~ 5 nm calculated using broadening of the (100)Zr reflection by the Scherrer formula. The interpretation of the electron diffraction reflections (Fig. 3b) confirmed the
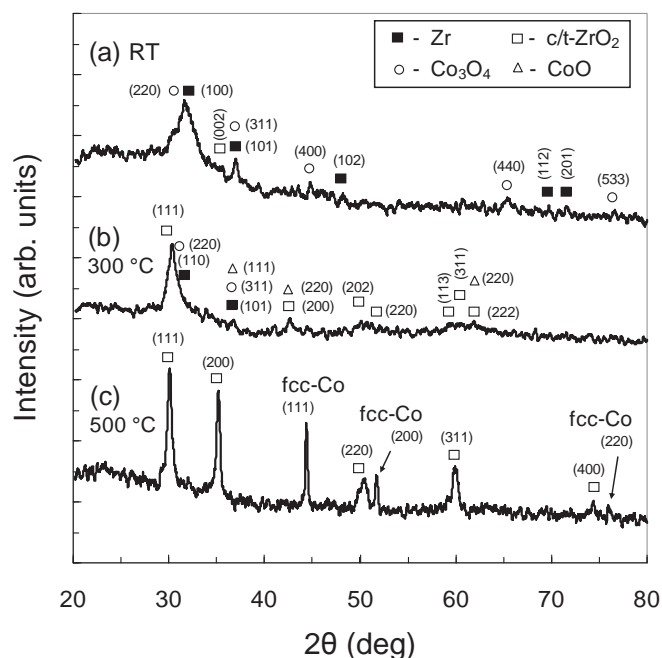

Fig. 2. Typical XRD patterns of the initial Zr/Co$_3$O$_4$ bilayers (a) and the synthesized Co−ZrO$_2$ nanocomposites after annealing at 300 °C (b), 500 °C (c).
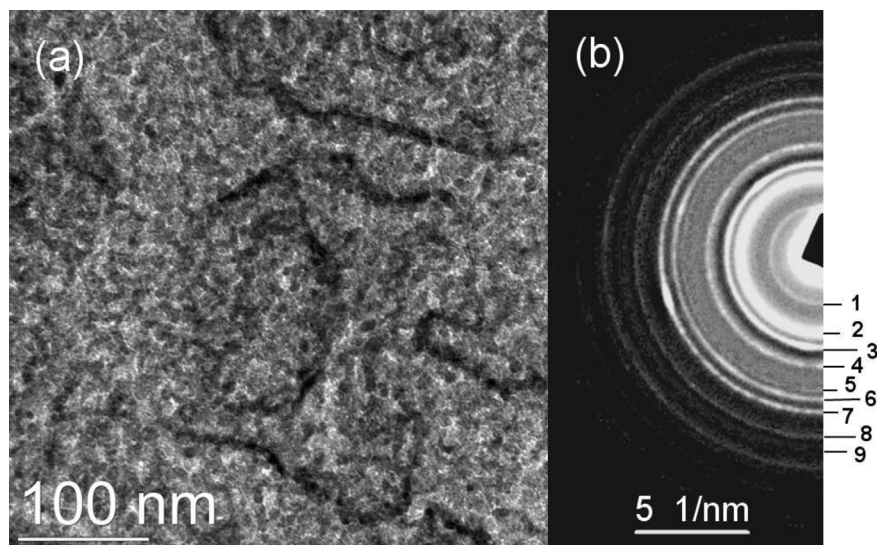
Fig. 3. TEM image (a) and electron diffraction pattern (b) of the initial Zr/Co_3O_4 sample.

coexistence of α-Zr and Co_3O_4 (see Table 1) in the initial Zr/Co_3O_4 films. Fig. 4 shows a typical TEM image, selected area electron diffraction pattern (SAED) of the Co–ZrO_2 film after annealing at 500 °C. The average atomic number for the ZrO_2 phase is lower than the atomic number of Co thus the ZrO_2 region appears brighter on the TEM image (Fig. 4a) than the Co region. The dark regions correspond to the Co grains and the light region - to the ZrO_2 matrix. The TEM observations (Fig. 4a) indicate that the Co nanoparticles have a shape resembling a sphere and were uniformly distributed in the reaction product. The TEM image, SAED pattern (Fig. 4) and electron diffraction analysis suggests that the final reaction product are hcp-Co + fcc-Co nanoparticles embedded in polycrystalline m-ZrO_2 + c/t-ZrO_2 matrix (Table 2). From Fig. 4a it follows that the average diameter of the Co nanoparticles is 20 nm, which is comparable with the superparamagnetic critical size, which is on the order of 20 nm for the Co nanoparticles [42]. However Co nanoparticles with a size below 10 nm are disregarded in the histogram, because it is impossible to obtain a high resolution TEM image due to the film thickness (50 nm). This suggests that all the synthesized Co–ZrO samples contain some amount of superparamagnetic Co nanoparticles. An important point is that the histogram is presented for a film thickness of 50 nm and it may be different from the histograms with film thicknesses of 300–400 nm, which were used for the magnetic, electrical resistance and magnetoresistance investigations.

3.3. Magnetic and magnetoresistance properties

In the Co–ZrO_2 nanocomposites after annealing at 500 °C more

than 80% of Co was reduced and thus it had high saturation magnetization (~500 emu/cm^3). The hysteresis loop yielded a typical hysteresis loop of the original Co film (before oxidation) with the coercivity ~ 130 Oe (Fig. 1a). The hysteresis loop achieved saturation at $H_S = 500$ Oe $> H_C = 130$ Oe. This clearly demonstrates the contribution of the superparamagnetic Co particles and disordered spins at Co/ZrO_2 interfaces into the hysteresis loop besides the contribution of the ferromagnetic particles. This result is in good agreement with the results from the TEM analysis, where superparamagnetic Co nanoparticles were assumed. The relatively large value of the ratio M_r to M_S equal 0.62 (where M_r is magnetic remanence) indicates that the Co nanoparticles consisted of randomly oriented equiaxial grains with cubic magnetocrystalline anisotropy [43].

The Co–ZrO_2 samples exhibited negative tunneling magnetoresistance (TMR) which is a characteristic property of granular ferromagnetic metal/insulator nanocomposites. It is known that spin-depended scattering of the conduction electrons between ferromagnetic nanogranules caused giant TMR in these nanocomposites below the percolation threshold (dielectric regime) [44–47,26]. For the Co–ZrO_2 granular films which had been prepared by pulsed laser deposition the maximum TMR was about 7% at 50 kOe and saturation magnetization was <50 emu/cm^3 [26]. In contrast to these samples the Co–ZrO_2 nanocomposite films which had been prepared by the thermite method revealed very weak negative magnetoresistance about 0.07% at 4.5 kOe and the high saturation magnetization M_S ~500 emu/cm^3 at room temperature.

3.4. In situ electron diffraction study of the Co–ZrO_2 thermite reaction in the Zr/Co_3O_4 thin films

In the initial state the Zr/Co_3O_4 films contained α-Zr and Co_3O_4 layers, as evidenced by the TEM image and corresponding SAED pattern (Fig. 3 and Table 1). The structural changes in the initial Zr/Co_3O_4 bilayer and the formation of the Zr–Co_3O_4 nanocomposite, monitored in the *in situ* heating electron diffraction experiment, is shown in Fig. 5a,b (see the indexing of the diffraction reflections in Table 3a,b). The analysis of the SAED patterns reveals that CoO and amorphous ZrO_2 started forming at 260 °C. This examination proves that the initiation temperature T_{in} of the reaction between Zr and Co_3O_4 was below 260 °C. It is in good agreement with the annealing investigation which indicates that the initiation

Table 1
Indexing the diffraction reflections in Fig. 3b.

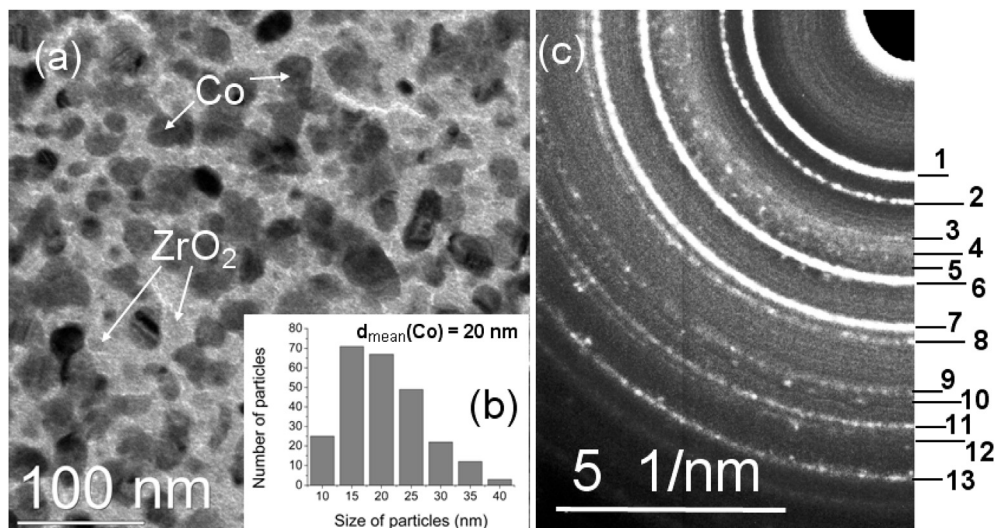| Rings	Co_3O_4	α-Zr
1	(111)	
2	(220)	(100)
3	(311)	(101)
4	(400)	(102)
5	(422)	(110)
6	(511)	(103)
7	(440)	(112)
8	(622)	(202)
9	(711)	

Fig. 4. TEM image (a) of Co nanoparticles embedded in the ZrO$_2$ matrix, (b) histogram of Co nanopartcles size distribution obtained from the TEM image (a), and (c) electron diffraction pattern of the Co—ZrO$_2$ film after annealing at 500 °C.

Table 2
Indexing the diffraction reflections in Fig. 4b.

Rings	m-ZrO$_2$	c/t-ZrO$_2$	Hcp-Co	Fcc-Co
1	(-111) (111)	(111)		
2	(200)	(002) (200)		
3			(100)	
4			(002)	(111)
5			(101)	
6	(122) (221)	(202) (220)		(200)
7	(213) (312)	(311)		
8	(023) (321)		(102)	
9	(041)	(004) (400)	(110)	(101)
10	(-232)	(114)		
11	(-313)	(420)	(103)	
12	(242)	(421)		(311)
13		(511)	(004)	(222)

Table 3
Indexing the diffraction reflections (a) in Fig. 5a at 300 °C and (b) in Fig. 5b at 500 °C.

(a)

Rings	m-ZrO$_2$	c/t-ZrO$_2$	CoO
1	(111)		
2	(-111)	(111)	
3	(200)	(002) (200)	(111)
4			(200)
5	(213) (312)	(311)	(220)
6	(023) (321)		
7	(041) (004)	(004) (400)	(311)
8	(242)	(421)	(400)
9		(511)	(331)
10			(422)

(b)

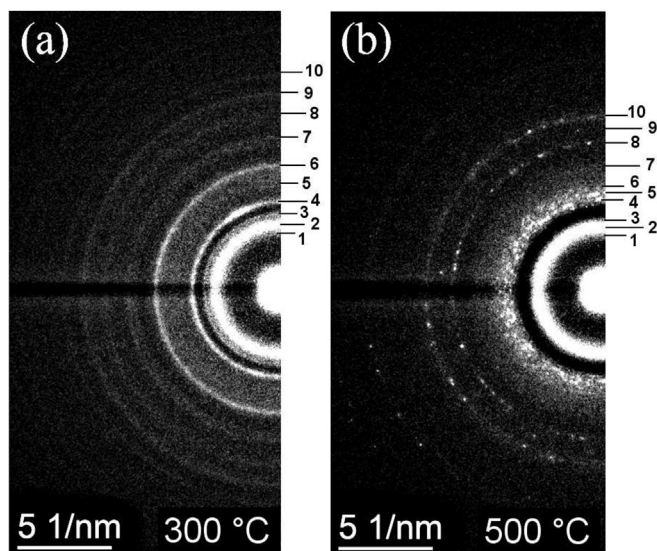| Rings	m-ZrO$_2$	c/t-ZrO$_2$	Hcp-Co	Fcc-Co
1	(111)			
2	(-111)	(111)		
3	(200)	(002)		
4			(002)	(111)
5			(101)	
6	(122) (221)	(202) (220)		(200)
7	(213) (312)	(311)		
8			(110)	(220)
9	(314)	(420)	(103)	
10		(422)	(004)	(222)

Fig. 5. Electron diffraction patterns of the Co—ZrO$_2$ film obtained at 300 °C (a) and 500 °C (b).

temperature T$_{in}$ ~250 °C (Fig. 1). With increasing the temperature up to 300 °C the Co$_3$O$_4$ reflections gradually disappeared from the SAED patterns and the polycrystalline reflections of the hcp-Co began to form above 400 °C. The existence of fcc-Co cannot be excluded due to the overlap of its main diffraction reflections with those of hcp-Co. The reflections of the CoO phase completely disappeared at 500 °C and the SAED pattern revealed hcp-Co, fcc-Co and m-ZrO$_2$, c/t- ZrO$_2$ phases (Fig. 5b and Table 3b). The sample cooling to room temperature did not change the phase composition and final reaction product contained hcp-Co, fcc-Co and m-ZrO$_2$, c/t- ZrO$_2$. This result is in good agreement with the final reaction product for the TEM samples obtained by annealing at 500 °C (Fig. 4 and Table 2). While the evidence of the Co formation was apparent from *in situ* heating electron diffraction experiment and XRD studies at temperatures higher 400 °C, the magnetic measurements clearly show the Co formation starting at the initiation temperature

T_{in} ~250 °C. The most plausible hypothesis is that above T_{in} ~250 °C Co grains started growing with the fine-dispersed structure which was not detected by the SAED and XRD experiments.

Notice that in the samples with the thickness of 50 nm (prepared for the TEM and *in situ* heating electron diffraction studies) stable hcp-Co and m-ZrO_2 phases were formed, but in the samples for magnetic and electrical investigations with the thickness of above 300—400 nm the high temperature fcc-Co and c/t- ZrO_2 phases, metastable at room temperature, were formed. A possible reason for the formation of the hcp-Co and m-ZrO_2 phases is stress relaxation in the thin layers that created favourable conditions for the equilibrium formation hcp-Co and m-ZrO_2 nanoclusters. However, in the thick layers the reaction stresses insignificantly relaxed and arrested the high temperature fcc-Co and c/t- ZrO_2 phases which were the product of reaction (1).

From the *in situ* heating electron diffraction experiments it follows that the reaction mechanism proposed involves CoO formation in the 260 °C - 500 °C (Table 3a) temperature range and therefore the existence of intermediate reactions (4), (5):

$$2Co_3O_4 \rightarrow CoO + O_2 \qquad (4)$$

$$2CoO + Zr \rightarrow 2Co + ZrO_2 \qquad (5)$$

The intermediate reactions often accompany the main reaction in different thermite systems including the classical thermite reaction between Fe_2O_3 and Al (Goldschmidt reaction) [48—50]. Recently we showed that the intermediate reactions were also present in the thermite reaction between Fe_2O_3 and Zr [30].

As is known, thin film solid state reactions are characterizes by the initiation temperature T_{in} and the first phase arising in the film interface when the temperature of a sample T_S exceeds T_{in} ($T_S > T_{in}$) [51—54]. We noticed that the initiation temperature T_{in} ~250 °C of Reaction (1) coincided with the initiation temperature of the thermite reaction in the Zr/Fe_2O_3 thin film [30]. It is common knowledge that the driving force of Al-based thermite reactions is the big negative heat of Al_2O_3 formation ($\Delta H_f = -1676$ kJ/mol). It is reasonable to suggest that the driving force of Zr-based reactions is the negative heat of ZrO_2 formation ($\Delta H_f = -1080$ kJ/mol). Therefore, different reaction systems which are controlled by ZrO_2 synthesis must have the same initiation temperature T_{in} ~250 °C. Indeed, the value T_{in} ~250 °C is in good agreement with the initiation temperature T_{in} ~250 °C in Zr/CuO nanothermite mixture [55] and with the study where the ZrO_2 nanoparticles were obtained by glycothermal processing [56]. In these papers [55,56] using the curves of differential thermal analysis (DTA), thermogravimetric analysis (TGA), and differential scanning calorimetry (DSC), the initiation temperature T_{in} ~250 °C was defined as the temperature at which heat release started.

Based on all the above, it can be concluded that the final product of the thermite reaction in the Zr/Co_3O_4 thin films contained Co nanoparticles above and below the superparamagnetic critical size embedded into a dielectric ZrO_2 matrix. The particle size of Co during the thermite reaction in the Zr/Co_3O_4 thin films strongly depended on the experimental conditions such as the heating rate and annealing time. The synthesized Co—ZrO_2 samples had good temperature stability and these samples did not change the magnetic properties over 8 months at room temperature. Therefore, the choice of the heating rate, the annealing temperature and annealing time determined the structural and magnetic properties of the nanocomposite Co—ZrO_2 thin films.

4. Summary

In summary, the Co—ZrO_2 ferromagnetic nanocomposites were synthesized using a new thermite reaction between Zr and Co_3O_4 thin films. The initial Zr/Co_3O_4 films were obtained by the Co films oxidation and sequential deposition of a Zr layers. Thermite reaction (1), using Zr and Co_3O_4 films as a fuel and an oxidizer in Zr/Co_3O_4 bilayers, started above the initiation temperature $T_{in} = 250$ °C. At the annealing temperatures above 300 °C the partial transformation (2) from Co_3O_4 to CoO occurred and thermite reaction (4) between CoO and Zr started. After 500 °C thermite reactions in the Zr/Co_3O_4 films finished and showed a high level of Co reduction (>80%). The final products with a film thickness of 50 nm contained Co nanograins with an average grain size of 20 nm uniformly distributed in the dielectric ZrO_2 matrix. The thermite method provides a promising route to the formation of Co—ZrO_2 ferromagnetic nanocomposite thin films having low initiation temperature, soft magnetic properties, high magnetization and good chemical stability.

References

[1] X. Batlle, A. Labarta, J. Phys. D. Appl. Phys. 35 (2002) R15—R42.
[2] A. Pucci, G. Clavel, M.-G. Willinger, D. Zitoun, N. Pinna, J. Phys. Chem. C 113 (2009) 12048—12058.
[3] T. Wen, K.M. Krishnan, J. Phys. D. Appl. Phys. 44 (2011), 393001-1-393001-24.
[4] J.T. Jiang, X.J. Wei, C.Y. Xu, Z.X. Zhou, L. Zhen, J. Magn. Magn. Mater. 334 (2013) 111—118.
[5] M. Baikousi, O. Kostoula, I. Panagiotopoulos, T. Bakas, A.P. Douvalis, I. Koutselas, A.B. Bourlinos, M.A. Karakassides, Thin Solid Film. 520 (2011) 159—165.
[6] J. Okabayashi, S. Kono, Y. Yamada, K. Nomura, AIP Adv. 1 (2011), 042138-1-042138-6.
[7] A. Butera, J.N. Zhou, J.A. Barnard, J. Appl. Phys. 87 (2000) 5627—5629.
[8] C. Chen, O. Kitakami, S. Okamoto, Y. Shimada, J. Appl. Phys. 86 (2161) (1999) 2161—2165.
[9] J. Gómez, A. Butera, J.A. Barnard, Phys. Rev. B 70 (2004), 054428-1-054428-9.
[10] O. Santini, D.H. Mosca, W.H. Schreiner, R. Marangoni, J.L. Guimaraes, F. Wypych, A.J.A. de Oliveira, J. Phys. D. Appl. Phys. 36 (2003) 428—433.
[11] X. Ni, J. Li, J. Alloy. Compd. 558 (2013) 62—67.
[12] X. Ni, J. Ma, J. Li, D. Jiao, J. Huang, X. Zhang, J. Alloy. Compd. 468 (2009) 386—391.
[13] Y. Chen, A. Li, Y. Li, J. Li, G. Dai, O. Fangping, X. Xiong, RSC Adv. 5 (2015) 35929—35933.
[14] D. Fang, K. Huang, Z. Luo, Y. Wang, S. Liu, Q. Zhang, J. Mater. Chem. 21 (2011) 4989—4994.
[15] P. Manivasakan, V. Rajendran, P. Ranjan Rauta, B.B. Sahu, B.K. Panda, J. Amer. Ceram. Soc. 94 (2011) 1410—1420.
[16] A. Buyukaksoy, T. Fürstenhaupt, V.I. Birss, Nanoscale 7 (2015), 8428—4837.
[17] N. Zink, F. Emmerling, T. Häger, M. Panthöfer, M.N. Tahir, U. Kolb, W. Tremel, Dalton Trans. 42 (2013) 432—440.
[18] S. Ostanin, A. Ernst, L.M. Sandratskii, P. Bruno, M. Däne, I.D. Hughes, J.B. Staunton, W. Hergert, I. Mertig, J. Kudrnovský, Phys. Rev. Lett. 98 (2007), 016101-1-016104-4.
[19] N.H. Hong, M.B. Kanoun, S. Goumri-Said, J.-H. Song, E. Chikoidze, Y. Dumont, A. Ruyter, M. Kurisu, J. Phys. Condens. Mater 25 (2013), 436003-1-436003-7.
[20] A. Pucci, G. Clavel, M.-G. Willinger, D. Zitoun, N. Pinna, J. Phys. Chem. 113 (2009) 12048—12058.
[21] V.V. Kriventsov, D.I. Kochubey, YuV. Maximov, I.P. Suzdalev, M.V. Tsodikov, J.A. Navio, M.C. Hidalgo, G. Colón, Nucl. Instrum. Meth. Phys. Res. A 470 (2001) 341—346.
[22] A. Debernardi, D. Sangalli, A. Lamperti, E. Cianci, P. Lupo, F. Casoli, F. Albertini, L. Nasi, R. Ciprian, P. Torelli, J. Appl. Phys. 115 (2014), 17D718-1-17D718-3.
[23] F. Legorreta Garcia, V.G. de Resende, E. De Grave, A. Peigney, A. Barnabé, C. Laurent, Mater. Res. Bull. 44 (2009), 1311—1301.
[24] M. García del Muro, Z. Konstantinović, M. Varela, X. Batlle, A. Labarta, J. Magn.

Magn. Mater 316 (2007) 103—105.

[25] C. Clavero, B. Sepúlveda, G. Armelles, Z. Konstantinović, M. García del Muro, A. Labarta, X. Batlle, J. Appl. Phys. 100 (2006), 074320-1-074320-5.

[26] Z. Konstantinović, M. García del Muro, M. Kovylina, X. Batlle, A. Labarta, Phys. Rev. B 79 (2009), 495304-1-094201-5.

[27] M. García del Muro, Z. Konstantinović, X. Batlle, A. Labarta, J. Phys. D. Appl. Phys. 46 (2013), 045418-1-045418-9.

[28] J. Shin, A. Goyal, C. Cantoni, J.W. Sinclair, J.R. Thompson, Nanotechnology 23 (2012), 1555602-1-1555602-6.

[29] V.G. Myagkov, I.A. Tambasov, O.A. Bayukov, V.S. Zhigalov, L.E. Bykova, YuL. Mikhlin, M.N. Volochaev, G.N. Bondarenko, J. Alloy. Compd. 612 (2014) 189—194.

[30] V.G. Myagkov, L.E. Bykova, O.A. Bayukov, V.S. Zhigalov, I.A. Tambasov, S.M. Zharkov, A.A. Matsynin, G.N. Bondarenko, J. Alloy. Compd. 636 (2015) 223—228.

[31] L.L. Wang, Z.A. Munir, Y.M. Maximov, J. Mater. Sci. 28 (1993) 3693—3708.

[32] E.L. Drezin, Prog. Energy Combust. Sci. 35 (2009) 141—167.

[33] Y. Yang, D.-r. Yan, Y.-c. Dong, X.-g. Chen, L. Wang, Z.-h. Chu, J.-x. Zhang, J.-n. He, J. Alloy. Compd. 579 (2013) 1.

[34] K.J. Blobaum, M.E. Reiss, J.M. Plitzko, T.P. Weihs, J. Appl. Phys. 94 (2003) 2915—2922.

[35] P. Zhu, J. Jiao, R. Shen, Y. Ye, Shuai Fu, D. Li, J. Appl. Phys. 115 (2014), 194502-1-194502-5.

[36] E.J. Mily, A. Oni, J.M. LeBeau, Y. Liu, H.J. Brown-Shaklee, J.F. Ihlefeld, J.-P. Maria, Thin Solid Film. 562 (2014) 405—410.

[37] M. Petrantoni, C. Rossi, L. Salvagnac, V. Conédéra, A. Estève, C. Tenailleau, P. Alphonse, Y.J. Chabal, J. Appl. Phys. 108 (2010), 084323-1-084323-5.

[38] V.G. Myagkov, V.S. Zhigalov, L.E. Bykova, G.N. Bondarenko, J. Magn. Magn. Mater. 305 (2006) 534—545.

[39] B.I. Shklovskii, A.L. Efros, Electronic Properties of Doped Semiconductors, Springer Verlag, Berlin, 1984.

[40] N.F. Mott, Conduction in Non-crystalline Materials, Oxford University Press, Oxford, 1987.

[41] C.A. Neugebauer, M.B. Webb, J. Appl. Phys. 33 (1962) 74—82.

[42] A.I. Gusev, A.A. Rempel, Nanocrystalline Materials, Cambridge International Science Publishing, 2004, p. p.351.

[43] J.H. Fendle (Ed.), Nanoparticles and Nanostructured Films: Preparation, Characterization and Applications, WILEY_VCH Verlag GmbH & Co KGaA, NY, 1998.

[44] S. Mitani, H. Fujimori, K. Takanashi, K. Yakushiji, J.-G. Ha, S. Takahashi, S. Maekawa, S. Ohnuma, N. Kobayashi, T. Masumoto, M. Ohnuma, K. Hono, J. Magn. Magn. Mater. 198—199 (1999) 179—184.

[45] A. Milner, A. Gerber, B. Groisman, M. Karpovsky, A. Gladkikh, Phys. Rev. Lett. 76 (1996) 475—478.

[46] S. Sankar, A.E. Berkowitz, D.J. Smith, Phys. Rev. B 62 (2000) 14273—14278.

[47] A. García-García, J.A. Pardo, P. Štrichovanec, C. Magén, A. Vovk, J.M. De Teresa, G.N. Kakazei, Y.G. Pogorelov, L. Morellón, P.A. Algarabel, M.R. Ibarra, Appl. Phys. Lett. 98 (2011), 122502—1-122502-3.

[48] Y. Yang, Y.-c. Dong, X.-g. Chen, L. Wang, Z.-h. Chu, J.-x. Zhang, J.-n. He, J. Alloy. Comp. 579 (2013) 1—6.

[49] A. Babakhani, E. Zahabi, H.Y. Mehrabani, J. Alloy. Comp. 514 (2012) 20—24.

[50] J.L. Chen, H.H. Hng, Y.W. Lee, S.W. Du, N.N. Thadhani, Combust. Flame 157 (2010) 2241—2249.

[51] J.M. Poate, K.N. Tu, J.W. Mayer (Eds.), Thin Films-interdiffusion and Reaction, Willey-Interscience, New York, 1978.

[52] E.G. Colgan, Mater. Sci. Rep. 5 (1990) 1—44.

[53] R. Pretorius, C.C. Theron, A. Vantomme, J.W. Mayer, Crit. Rev. Solid. State Mater. Sci. 24 (1999) 1—62.

[54] T. Laurila, J. Molarius, Crit. Rev. Solid. State Mater. Sci. 28 (2003) 185—230.

[55] E.J. Mily, A. Oni, J.M. LeBeau, Y. Liu, H.J. Brown-Shaklee, J.F. Ihlefeld, J.-P. Maria, Thin Solid Film. 562 (2014) 405—410.

[56] J.-S. Kim, D.-H. Lee, S. Kang, D.-S. Bae, H.-Y. Park, M.-K. Na, Trans. Nonferrous Met. Soc. China 19 (2009) s88—s91.